Volume 1 | Number 1 | Jan 2013 | Pages 1–100

Nanoscale

www.rsc.org/nanoscale

ROYAL SOCIETY OF CHEMISTRY

ROYAL SOCIETY OF CHEMISTRY

www.rsc.org/nanoscale

Nanoscale

Tailoredgold nanostructure arraysas catalysts for oxygen reductionin alkaline media and single molecule SERS platform

Wojciech Nogala,* PalanisamyKannan, Sylwester Gawinkowski, Martin Jönsson-Niedziolka, Magdalena Kominiak, Jacek Waluk and Marcin Opallo

Although plenty functional nanomaterials are widely applied in science and technology, cost-efficient, controlled and reproducible fabrication of metallic nanostructures is a considerable challenge. Automated electrorefining by scanning electrochemical microscopy (SECM) provides an effective approach to circumvent some drawbacks of traditional homogeneous syntheses of nanoparticles, providing precise control over amount, time and place of reactant delivery. The precursor is just a raw metal, which is the most economically viable source. This approach ensures reproducibility, and the opportunity for fabrication of micropatterns, which can be rapidly analyzed by scanning probe techniques. Here, a cost-effective methodology of preparation of naked (ligand-free) metallic nanostructures, from polycrystalline gold using a moving microelectrode is presented. Automated micropatterning of bare gold on indium tin oxide (ITO) demonstrates the versatility of this method to tune the size and shape of the nanostructures. The morphology of the obtained materials, and thus their catalytic and plasmonic properties can be tuned by the electrorefining parameters. Programmable fabrication of sample microarrays by microprinting, followed by comparative SECM studies or spectroscopic analysis allows quick optimization and characterization for specific purposes. Electrocatalytic oxygen reduction in alkaline media and surface-enhanced Raman spectroscopy (SERS) of single porphycene molecules are presented as model examples.

Introduction

A wide range of nanostructured materials have been employed in various technological fields, such as diagnosis and therapy of diseases,[1,2] pathogenic bacteria combat,[3] drug delivery,[4] (photo)catalysis,[5,6] energy conversion and storage,[7] photovoltaics,[8] biosensing,[9] optoelectronics,[10] and water treatment.[11] Among these materials, metallic nanostructures (NS) are especially popular and important in the applications of electrochemical energy storage and conversion, because of their unique structural features offering both high surface area and large amount of catalytically active sites.[7] Due to the emergence of alkaline anion exchange polymeric membranes for fuel cells in last decade,[12] metallic NS have gained high importance as catalysts.[13] Numerous abundant non-platinum metals, *e.g.* gold, silver, copper or nickel exhibit superior stability in alkaline environment. Both organic fuel oxidation[14] and oxygen reduction reaction (ORR)[15] are catalytically enhanced in alkaline media. However, a significant overpotential is still necessary to overcome the thermodynamic barrier of these processes.

Nanostructured gold (AuNS) appears to be one of the most interesting candidates for efficient nanocatalyst in alkaline fuel cells.[16] In contrast to other metals, gold exhibits excellent resistance to corrosion, demonstrated by its inability to react with atmospheric gases. No oxide layer causing catalytic deactivation is spontaneously created on gold surfaces. Another important property of AuNS is the ability of conduction band electrons to oscillate collectively under the influence of electromagnetic wave in visible light range (localized surface plasmon resonance). These locally oscillating electrons enhance local electromagnetic field that interacts with adsorbed molecules. This results in the enhancement of scattered radiation, which is utilized in surface-enhanced Raman spectroscopy (SERS). This technique is so sensitive that even a single molecule can be detected.[17]

Both chemical activity and Raman signal enhancement are known to be very sensitive to the morphology of NS. Surface facets, edges and corners determine the catalytic activity. Theoretical studies show that low coordination number surface atoms, such as these occupying edges and corners of NS, are the sites of increased catalytic activity.[18] Sharp edges and tips significantly promote electric field enhancement, which is useful in SERS (so called "hot spots").[19] Decreasing the nanoparticle size results in the increase of the surface/volume ratio and higher number of low coordination surface atoms. Therefore smaller NS should exhibit more efficient catalytic

properties. However, there are indications that, at some point, minimization of NS size leads to deterioration of their applicable properties and bigger objects are more desired.[20,21] Also plasmonic properties strongly depend on the size and shape of nanostructures.[22] Therefore, one needs to optimize the NS preparation procedure to obtain a material for a particular application.

Liquid phase homogeneous synthesis of gold nanoparticles requires a gold precursor (*e.g.* $AuCl_4^-$), and a reducing agent (*e.g.* $NaBH_4$), but also organic molecules to create a protecting layer on the nanoparticles surfaces, preventing further growth and aggregation.[23] Surface ligands can also provide various functionalities.[1,24] However, their presence may decrease catalytic activity, affect plasmonic properties and hinder an access of the analyte to the metal surface. Moreover, stabilizers may introduce undesired bands in SERS spectra[25] and affect catalytic properties of NS.[6] Unmodified metallic NS favorable for both catalysis and SERS can be prepared by heterogeneous processes, *e.g.* electrodeposition.[26] Their further growth is stopped by switching off the voltage driving the electroreduction of the precursor present in the electrolyte. NS obtained in this way are directly anchored to the support, thus protection against aggregation is not necessary, and unmodified NS can be prepared. A special variant of electrodeposition is electrorefining,[27] a process utilized for industrial purification of metals. A metallic anode is oxidized with *in-situ* creation of metal ions which act as a precursor for electrodeposition on the cathode. This can be realized in a microscopic scale using tip generation/substrate collection mode[28] or direct mode[29] of SECM.[30] Deposition of gold can be realized as faradaic[31] or electroless[32] process. The morphology of the obtained deposit, and thus its catalytic and plasmonic properties, depend on fabrication conditions, such as temperature, overpotential, current density, solution composition, and cathode morphology. So far, no reliable way to design the preparation procedure of the most efficient catalyst or SERS support is known. Development of such a procedure is highly desirable.

Localized electrorefining allows quick fabrication of microscopic patterns where only a small amount of raw metal is used. A number of various NS can be prepared on a single support and studied instantaneously for their catalytic activity by SECM or for SERS applicability by Raman microspectroscopy. Simultaneous examination of micropatterned NS provides reliable comparative results and direct clues for "know-how" to prepare desired materials. An additional advantage of AuNS preparation directly from polycrystalline metallic Au source is the cost-efficiency of this approach. This is because metallic gold is much cheaper than gold in the chemical compounds used for AuNS synthesis.

Here we demonstrate automated micropatterning of a broad range of bare AuNS on ITO and a comparative SECM study of their catalytic activity towards oxygen reduction in alkaline electrolyte. The applicability of the materials as a SERS support was also tested and optimized.

Experimental

All electrochemical experiments were performed using a CHI900B SECM (CH Instruments, Inc.) mounted on a Nikon MA200 inverted microscope using a homemade adapter. A gold microelectrode served as a moveable first working electrode, ITO coated glass (sheet resistance 8-12 Ω/sq., Delta Technologies, Ltd.) as a second working electrode, Ag|AgCl|3M KCl as reference, and platinum wire as auxiliary electrodes were used for electrorefining and electroanalysis. Microelectrodes were prepared by sealing 100 μm or 25 μm Au wire (Alfa Aesar) into a borosilicate capillary using a PC-1 puller (Narishige) and polished with P2000 grit silicon carbide sandpaper. NaCl, KCl, K_2SO_4 (pure p.a., Chempur), KOH (99.99%, Sigma-Aldrich) were used as received for the preparation of solutions using water deionized by Elix system (Millipore). *Pc* was synthesized according to the procedure described in Ref.33. Three concentrations of *Pc* solution in ethanol (spectroscopic grade, Merck) were used for SERS measurements: 10^{-6} and 10^{-8} for optimization of the substrate for SERS applications, and 10^{-10} mol dm^{-3} for single molecule measurements. *Pc* solution was drop-casted on the sample covering a *ca.* 6 mm diameter circle and evaporated under ambient conditions. Maps of Raman spectra were recorded with 0.3 s accumulation time using a RenishawInVia microscope equipped with 100× objective (Leica, NA=0.85, measured focus diameter *ca.* 1.25 μm) and 633 nm HeNe laser whose power was set below 0.1 mW on the sample.

Results and discussion

AuNS were fabricated by using a gold microelectrode (100 μm diameter, metal source) positioned 20 μm above the ITO support. Utilizing the optical transparency of ITO one can control the distance between the source and the support with the help of an inverted optical microscope. The narrow depth of field of high magnification objectives (50×, 100×) allows the distance between the source and the support to be controlled with *ca.* 1 μm accuracy. No redox mediator, possibly affecting the nanostructure and the properties of the obtained deposits, is needed for vertical positioning of the microelectrode. Since there is no redox cycling between the microelectrode and the substrate during deposition, the amount of deposited metal can be determined from the measured faradaic charge. At moderate potentials, when no additional processes (*e.g.* oxygen reduction or chlorine evolution) occur, the faradaic currents recorded at the source and the support are related to gold electrodissolution,

$$Au^0 + 4Cl^- - 3e^- \rightarrow AuCl_4^-, \tag{1}$$

rate and electrodeposition,

$$AuCl_4^- + 3e^- \rightarrow Au^0 + 4Cl^-, \tag{2}$$

respectively. Despite possible 1-electron electrodissolution of the Au,[34,35] 3-electron processes (1 and 2) are commonly considered in the literature. These opposite processes are kinetically sluggish, *i.e.* a substantial electrochemical potential
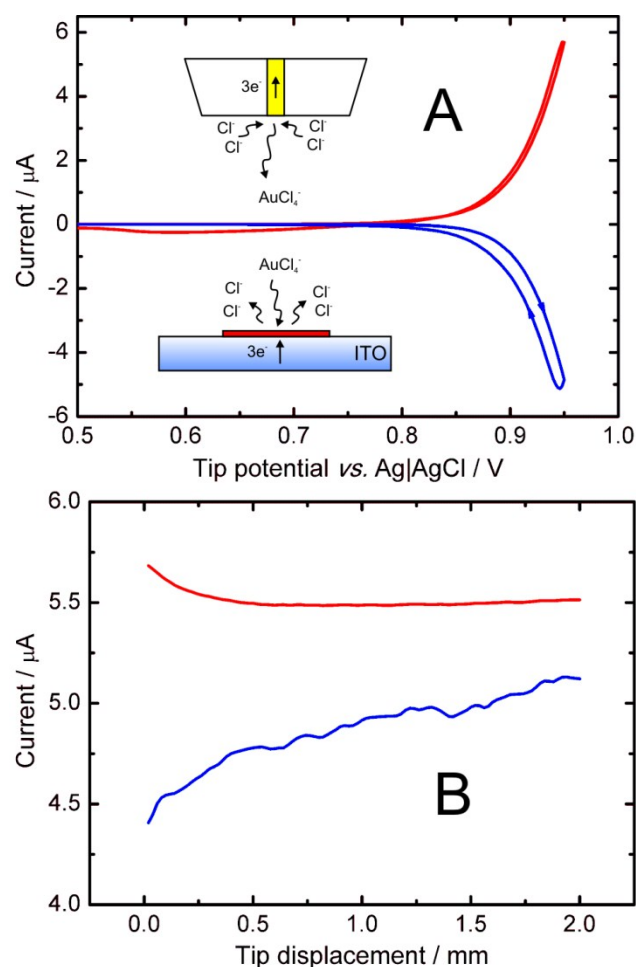
Fig. 1 (A) – Cyclic voltammogram of 100 μm diameter Au electrode (tip, red line) positioned 20 μm above the ITO electrode (substrate) polarized at +0.5 V. Blue line is the substrate current *vs.* tip potential. Electrolyte: 3 mol dm⁻³NaCl, Scan rate: 10 mV s⁻¹. The inset in figure (A) is a scheme of occurring processes (not to scale). (B) – Tip current (anodic, red line) and inverse of substrate current (cathodic, blue line) recorded during lateral tip movement 20 μm above the ITO substrate. Translation speed: 100 μm s⁻¹, tip potential: +0.95 V, substrate potential: -0.3 V.

difference is required to drive them. Anodic polarization of gold in aqueous solution in the absence of a complexing agent results in gold oxide formation (passivation) preventing its dissolution. Chloride ions facilitate electrodissolution of gold in water due to the much lower standard potential of processes (1) and (2) (0.99 V *vs.* SHE) than chlorine evolution (1.4 V vs. SHE) or water splitting (1.23 V vs. RHE).[35] In order to assure favorable conditions for gold electrodissolution (equation (1)) highly concentrated chloride solution (3 mol dm⁻³ NaCl) was used. Under these conditions electrodissolution of metallic gold occurs at potentials higher than *ca.* 0.85 V vs. Ag|AgCl (Figure 1A).

The kinetic limitation of process (1) allows the rate of dissolution to be controlled by potentiostatic polarization of the electrode. No current decay was observed when the electrode was moving parallel to the ITO surface (Figure 1B). This shows that the dissolution rate of the Au microelectrode can be controlled by potentiostatic polarization, *i.e.*, no galvanostatic polarization of the tip is necessary to maintain a stable dissolution rate. Electrodissolution of a

microelectrodeand the influence of electrode size to electrorefining are discussed in detail in Supporting Information S1.

We intended to obtain precisely localized Au deposits (just beneath the tip) with the highest possible collection efficiency. Therefore the Au microelectrode was positioned at a relatively short distance from the ITO (0.2 of its diameter). For 100 μm diameter electrode this distance is easy to set with the help of an optical microscope, and prevents formation of short circuit between the source and the support,[36] when the microelectrode is moving with velocity at least 50 μm s⁻¹. For slower velocities or shorter distances (source polarized at 0.95 V) a few attempts of electrorefining failed due to vertically growing gold microstructures leading to short circuit. Relatively slow electrodissolution of gold at 0.95 V (corresponding current density 70 mA cm⁻²) was chosen for localized 'injection' of AuCl₄⁻ without its oversaturation. The dissolution rate was ~0.24 μmol_Au cm⁻² s⁻¹ (~48 μg_Au cm⁻² s⁻¹), which corresponds to a hypothetic uniform source length (recession) rate of *ca.* 25 nm s⁻¹.This causes minor relative recession of a 100 μm microelectrode even during long-lasting experiments.However, application of a nanoelectrode would require frequent renewal of the electrode (see supporting information S1).

The cathodic curve in Figure 1A (dashed line) corresponds to Au electrodeposition (equation 2) recorded at the ITO substrate held at constant potential (+0.5 V) as a function of the tip potential. The collection efficiency under these conditions (20 μm distance and stationary source), calculated as the absolute ratio of the charge passed through the substrate to the charge passed through the source (tip) is $|q_S/q_T| \approx 0.87$. The remaining ~13% of dissolved Au diffuses towards the bulk electrolyte. No homogeneous reaction of AuCl₄⁻ is expected because of its stability in aqueous media. The collection efficiencies calculated for dynamic conditions (when the source moves parallel to the ITO surface) are slightly lower due to convection. A detailed discussion is available in Supporting Information S2.

Diffusion causes the obtained microbands to become a bit blurred and wider than the source microelectrode diameter. This effect is better visible for longer tip-to-sample distance (see the movie in Supporting Information S3). Nevertheless, the majority of the metal is deposited just beneath the source when the tip-to-sample distance is much shorter than the tip diameter (here 20 μm and 100 μm, respectively). Assuming that the metal is deposited mainly beneath the tip source, one can calculate the surface concentration of metal in deposited micro-bands using equation 3.

$$\Gamma = \frac{i_T \theta}{zF \phi_T v} \tag{3}$$

Where Γ is surface concentration (mol cm⁻²), i_T – tip current (A), ϑ – collection efficiency, z – number of electrons transferred per metal atom/ion (here 3), F – Faraday constant (96485 C mol⁻¹), ϕ_T – tip diameter (cm), v – tip translation velocity (cm s⁻¹). Collection efficiencies and surface concentrations of gold in electrorefinedmicrobands are listed in Table 1.

Table 1. Collection efficiencies and surface concentrations of Au in microbands obtained by localized electrorefining from 100 µm diameter Au microelectrode translated 20 µm above cathodically polarized ITO substrate. Tip potential: +0.95 V (corresponding current: 5.5 µA). Electrolyte: 3 mol dm^{-3} NaCl.

v [µm s^{-1}]	θ	Γ_{Au} [nmol cm^{-2}]	Γ_{Au} [µg cm^{-2}]
50	0.799 (±0.076)	304 (±29)	59.8 (±5.7)
100	0.712 (±0.037)	135 (±7)	26.6 (±1.4)
200	0,688 (±0.068)	65 (±6.5)	12.9 (±1.3)

The thicknesses of hypothetical uniform Au layers obtained at 50, 100, and 200 µm s^{-1} would be *ca.* 31, 13, and 6.7 nm, respectively. Electrodeposition without special electroplating additives, however, results in inhomogeneous deposits.[26] The growth of metallic crystals occurs as long as sufficiently negative potential is applied to the support and metal ions are delivered. In localized electrorefining at constant potential applied to the electrodes, metal ions are delivered to certain areas of the support, where the microelectrode is positioned. The amount of the precursor delivered to certain areas of the support is inversely proportional to the lateral tip velocity (equation 3). It is clearly seen in SEM images of electrorefined Au (Figure 2 and Supporting Information S4) that amount of deposited material is higher for slower tip velocities.

We made an attempt to estimate the amount of metal deposited on ITO substrate by analysis of SEM images (Figure 3). Detailed description of the procedure with discussion is available in Supporting Information S5. Surface concentration of electrorefined Au estimated by SEM images analysis (Figure 3A) is higher than that calculated using equation 3, even with hypothetic 100 % collection efficiency. This suggest that one-electron oxidation of Au is essentially involved in electrodissolution process:

$$Au^0 + 2Cl^- - e^- \rightarrow AuCl_2^- \qquad (4)$$
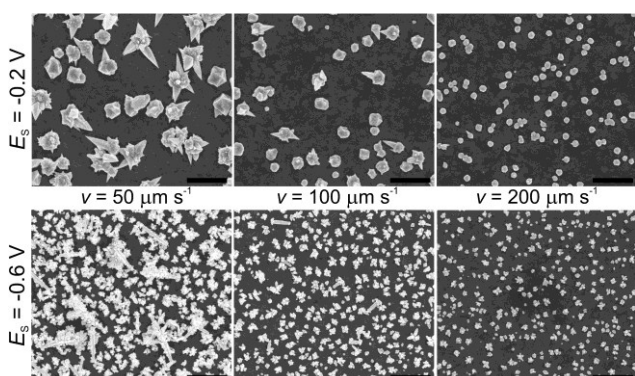
Fig 2 SEM images of AuNS prepared by localized electrorefining using 100 µm dia. Au microelectrode translating 20 µm above the ITO substrate polarized at -0.2 V (upper row) and -0.6 V (bottom row). Translation velocities: 50 µm s^{-1} (left column), 100 µm s^{-1} (center column), 200 µm s^{-1} (right column). Tip potential: +0.95 V. Electrolyte: aqueous 3 mol dm^{-3} NaCl. Horizontal full width of each image is 5 µm. Scale bars: 1 µm. Higher magnification images are available in Supporting Information S4.
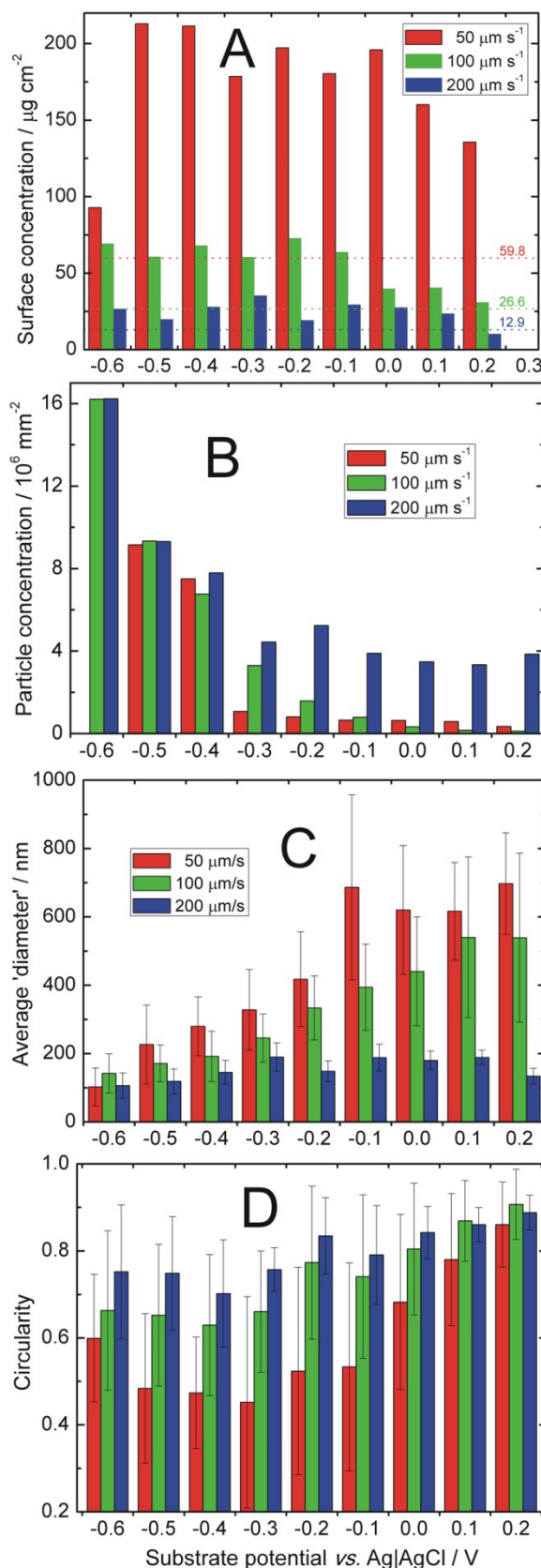
Fig. 3 Surface concentrations (A), particle concentrations (B), average sizes (C), and circularities (the ratios between the diameters of the inscribed and the circumscribed circles) (D) of AuNS obtained by analysis of their SEM images. Dotted lines in Figure correspond to surface concentrations of Au calculated using Faraday laws (equation 3)

Au(I) complexes with cyanide, sulfite and thiosulfate ligands are stable and used often as electroplating baths components.[26] Although the standard potential of the process (4) (1.11 V vs. SHE) is higher than that of the process from equations 1 and 2, partial formation of unstable $AuCl_2^-$ during electrodissolution of Au in chloride containing aqueous solution has been suggested.[34,35] Earlier studies of Au electrodissolution have shown, using SERS, the presence of $AuCl_2^-$ on the Au surface.[37] Besides rapid electrooxidation of $AuCl_2^-$ to $AuCl_4^-$, it can also undergoes disproportionation:[38]

$$3AuCl_2^- \rightarrow AuCl_4^- + 2Au^0 + 2Cl^-, \qquad (5)$$
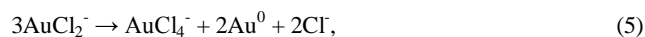
However, at Cl^- concentration as high as 3 mol dm^{-3} this is thermodynamically less favored (according to the Le Chatelier's principle). The $AuCl_2^-$ is likely to diffuse quickly to the ITO (just 20 μm beneath), where it is immediately reduced. This reaction consumes only one electron per Au atom and the amount of deposited Au from faradaic charge may be underestimated. Formation of $AuCl_2^-$ during electrorefining is more efficient in terms of electricity consumed.

More negative potential applied to the ITO results in higher number of nanoparticles per unit area (Figure 3B). However, the amount of the deposited material is similar for samples deposited at the same tip velocity. This is in accordance with potential-dependent kinetic limitation of the nucleation rate.[39] For higher substrate potentials (-0.3 V ÷ +0.2 V) particle concentration is higher for samples prepared with faster tip translations. This means that at slower translations a part of nuclei connect together forming new growing NS. The average size of the Au particles obtained by localized electrorefining is controllable by the applied substrate potential and the tip translation rate (Figure 3C). However, for slower translation rates and extremely high overpotentials nucleation and further growth occur on numerous sites on the substrate surface, as well as on already growing particles, resulting in nanoparticulate aggregate formation (Supporting Information S4). Estimation of the number of nanoparticles from SEM images of these samples is less reliable.Therefore this parameter is not presented in figure 3B for NS obtained at v = 50 μm s-1 and E_S = -0.6V.The accessibility of active sites is expected to be lower, because some of them are not exposed to the substrate diffusing from the surrounding medium. We were not able to study electrorefining at a substrate potential more negative than -0.6 V vs. Ag|AgCl, because such polarization of ITO leads to alteration of its surface morphology[40] which might affect NS adhesion. Other electrode materials, *e.g.*, glassy carbon may be more suitable for Au electrorefining at extreme cathodic potentials.

Polarization of the substrate at higher potentials leads to a lower number of nucleation sites, and thus to a lower number of bigger particles. Their relatively low surface area may also lead to a lower number of exposed catalytically active sites. Therefore examination of catalytic applicability of the obtained materials requires independent measurements. Here, ORR in alkaline electrolyte has been chosen as a model reaction due to its sluggish kinetics and its importance as cathode reaction in alkaline fuel cells. This reaction is chemically reversible,

which allows it to be studied by SECM in feedback mode.[41] In this mode O_2 is generated at the SECM tip by OH^- oxidation. Oxygen generated at the tip diffuses to the sample, where it reduced, generating additional flux of hydroxide ions (Figure 4 inset). The concentration of OH^- above a surface exhibiting catalytic activity towards ORR increases, thus the anodic current recorded on the SECM tip positioned near a highly active surface is higher than when the tip scans above a surface exhibiting lower activity. The feedback current at constant tip-to-sample distance is a function of the reaction rate on the sample, and provides direct information about the sample catalytic activity.[30] The plot of tip current versus its lateral position, recorded during scanning across a set of Au stripes prepared by electrorefining at different sample potentials (Figure 4) reveals that each stripe exhibits different activity towards ORR in alkaline electrolyte, although each sample contains the same amount of Au per unit area. The decrease of the background current is due to probe deactivation caused by formation of oxide film on the Au polarized at constant potential.[41]The catalytic activity depends on the electrorefining potential and reaches maximum for the stripe deposited at -0.5 V. The stripes obtained at less cathodic potentials exhibit lower activity. This is in accordance with morphology of obtained structures. A lower number of larger particles per unit area contain a lower number of exposed Au atoms. Interestingly, the sample comprising smaller NS deposited at the most negative potential (-0.6 V) is less active than that deposited at -0.5 V. This behavior correlates with the sphericity of the particles (Figure 3D and Supporting Information S6). AuNS deposited at -0.6 V are smaller, but more circular, *i.e.* they contain less edges and corners, known as catalytic active sites.[18] This means that as small nanoparticles as possible are not necessarily desirable for catalytic application.[20]
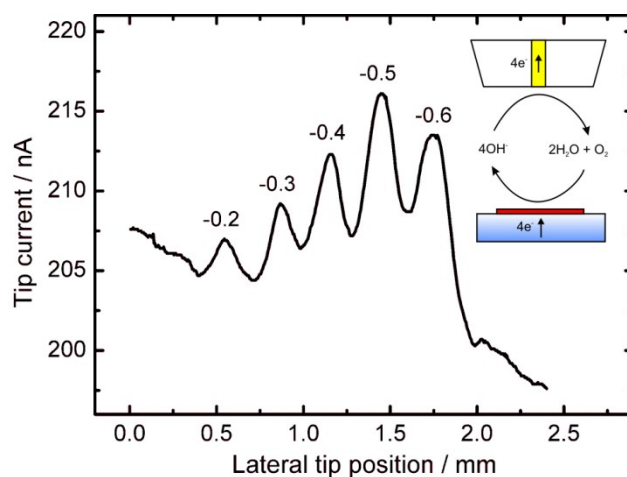
Fig 4 SECM line scan analysis result of the set of microstripes of AuNS obtained by localized electrorefining at various substrate potentials (marked in the figure) with Au source microelectrode translated at 50 μm s⁻¹. Other parameters of electrorefining as in Figure 2 caption. In analytical experiment 100 μm diameter Au microelectrode (tip) translated 20 μm above the sample perpendicular to microbands of AuNS at 10 μm s⁻¹. Tip potential: 1.3 V, Sample potential: -0.3 V, reference electrode: Ag|AgCl, electrolyte: aqueous 10 mmol dm⁻³ KOH + 0.1 mol dm⁻³ K₂SO₄. Inset: a scheme of feedback mode SECM study of ORR in alkaline solution.

An additional advantage of electrorefining at less negative substrate potential is lower electricity consumption.

Preparation of sets of samples or various two-dimensional shapes by localized electrorefining can be easily automated by batch processing or microprinting implemented in the SECM software (Supporting Information S7). A test sample printed this way was studied as a SERS support. Porphycene (*Pc*, Figure 5 inset), the structural isomer of porphyrin, was selected as a model system for these studies. *Pc* has attracted attention both in fundamental research and in various areas of potential applications ranging from cancer phototherapy[42] to molecular switches.[43] Contrary to porphyrin, *Pc*, due to a smaller inner cavity, does not coordinate metal atoms of nanostructures and gives clear SERS spectra. It also has high photostability, and well understood photophysics on metal surfaces.[43] SERS spectra of *Pc* averaged over (60×60) μm^2 maps with 1 μm step were compared with the unenhanced resonance Raman spectra of crystalline *Pc*. On the basis of the ratio of these signals and taking into account differences in excitation intensities, number of molecules in the objective focus, and the time of accumulation, the average SERS enhancement factor (EF) was estimated. The highly enhanced Stokes lines characteristic for this molecule are seen in the Raman spectrum in Figure 5A. The surface-averaged EF estimated for two concentrations of the *Pc* solution was 7.1×10^5 and 1.7×10^6 for 10^{-6} and 10^{-8} mol dm^{-3}, respectively.

The same size maps measured for the substrate before drop-casting of *Pc* on it presented no bands over the whole map, indicating that the substrate is chemically very clean, at least with respect to the substances whose Raman spectra can be enhanced to detectable levels.

Similarly to catalytic properties, SERS applicability of AuNS depends on the preparation conditions. In order to optimize the electrorefining process, for this purpose, we studied their influence on the distribution of *Pc* Raman signal using confocal Raman spectroscopy (see Supporting Information S8 for details). Au samples prepared at most negative potential applied to the ITO support (-0.6 V)

Fig 5 (A), SERS spectrum of porphycenepreadsorbed on AuNS prepared by localized electrorefining. (B), Time evolution of the 343 cm^{-1} band intensity. The spectra presented in (A) were recorded at time points indicated by dashed arrows.

and moderate tip translation velocity (100 μm s^{-1}) exhibit highest number of SERS hot spots and highest overall signal intensity. This behavior correlates with the substrate potential particle size dependency (Figure 3C). The smaller surface curvature radius of smaller nanostructures is known as loci of increased electromagnetic field resulting in enhanced Raman signal. Either faster (200 μm s^{-1}) or slower (50 μm s^{-1}) tip translations result in samples with less favorable SERS properties. The higher signal on samples prepared at moderate tip translation rate (100 μm s^{-1}) comparing to that recorded on samples deposited at faster translation rate (200 μm s^{-1}) may result from higher surface concentration of deposited Au. However, samples deposited at 50 μm s^{-1}, comprising more Au atoms per unit area, exhibit a lower Raman signal enhancement. This can be explained by formation of larger aggregates (see Figure 2). Their plasmon resonance wavelength is shifted out of the laser radiation frequency, and, as a result, the SERS signal drops significantly. Generally, inhomogeneous size and circularity distribution of all prepared NS widens their plasmon resonance wavelength range. This facilitates their plasmons excitation with not ideally adjusted laser wavelength.

The sample of AuNS exhibiting the highest surface concentration of highly enhancing "hot spots" (prepared at: E = -0.6 V, v = 100 μm s^{-1}) has been chosen for a single molecule (SM) SERS study. The sample was modified with *Pc* by drop-casting, using a highly diluted solution (10^{-10} mol dm^{-3}). A 0.5 μ droplet spread over *ca.* 6 mm diameter area of the sample corresponds on average to 1.2 *Pc* molecules in the objective focus. Considering the "coffee ring" effect,[44] affecting drop-casting deposition, the *Pc* real surface concentration is even lower. Moreover, the molecule can be registered only if it is situated in a very "hot" hot-spot. Under such conditions the observed SERS spectra can be assumed to originate from individual molecules. At a few sites, the spectra confirm the presence of the deposited compound (Figure 5A). Figure 5B presents typical behavior of time evolution of SM-SERS spectra, one step bleaching indicating a SM behavior. SM character of spectra was also proved by bi-analyte method.[45] The substrate was covered by the 1:1 mixture of Pc and its isotopologue with all hydrogen atoms at the periphery of the molecule exchanged with deuterons. SERS maps of such samples contained few percent points with the spectra of analyte in exclusively deuterated or undeuterated form. The absence of the SERS spectra representing mixture of the isotopologues provides single molecule regime.The estimated EF for the "hottest" SM SERS events is 10^{10}. The intensity of the bands characteristic for *Pc* varies with time, leading to complete extinction within a few tens of seconds. The time trace of the intensity of the most intense *Pc* band (343 cm^{-1}) extracted from the set of spectra recorded subsequently in the same point reveals stepwise changes. The signal had disappeared at once for 2 sec, and 15 sec later vanished permanently, also in a single step. Such signal alteration is probably caused by mobility of adsorbed molecules on the metal surface. The molecule can move out from the "hot spot" and back, change its orientation[42] or suffer photodecomposition due to intense
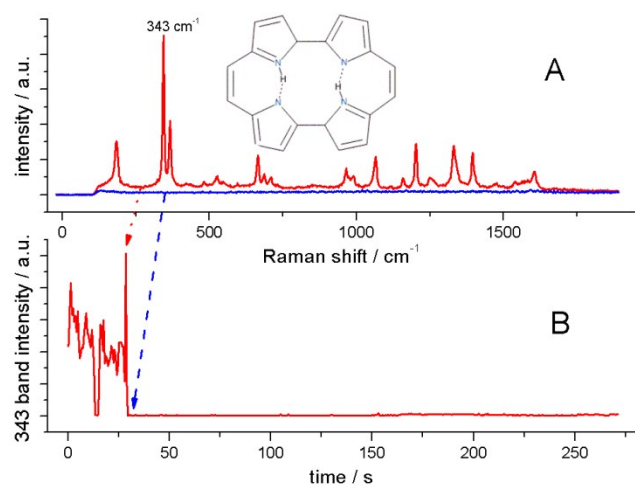
electromagnetic field in the hot-spot. Single step extinction and reappearance of the signal, as well as lack of its gradual or multi-step alterations suggest that only one porphycene molecule exhibiting Raman scattering enhanced by Au support was present within a laser beam.

Conclusions

A cost-effective methodology of preparation of bare gold nanostructures from a metal gold wire has been developed. This procedure relies on localized electrorefining using a translating microelectrode as scanning electrochemical microscopy tip. The morphology of the obtained materials, and thus their catalytic and plasmonic properties can be tuned by changing the electrorefining parameters, *i.e.*, the applied voltage and the source translation rate. Programmable fabrication of sample microarrays by microprinting followed by microscopic analysis allows quick optimization and characterization for specific purposes, with electrocatalytic oxygen reduction in alkaline media and Raman spectroscopy of single molecules presented as model examples. Comparison of the surface concentration of obtained gold nanostructures, evaluated by microscopic analysis, with the faradaic charge suggests a significant contribution of one-electron electrodissolution of gold in addition to the commonly reported three-electrons pathway.

Acknowledgements

References

1 A. J. Mieszawska, W. J. M. Mulder, Z. A. Fayad and D. P. Cormode, *Mol. Pharmaceut.*, 2013, **10**, 831.
2 J. Y. Yhee, S. Lee and K. Kim, *Nanoscale*, 2014, **6**, 13383.
3 Y. Luo, M. Hossain, C. M. Wang, Y. Qiao, J. C. An, L. Y. Ma and M. Su, *Nanoscale*, 2013, **5**, 687.
4 A. Latorre, C. Posch, Y. Garcimartin, A. Celli, M. Sanlorenzo, I. Vujic, J. Ma, M. Zekhtser, K. Rappersberger, S. Ortiz-Urda and A. Somoza, *Nanoscale*, 2014, **6**, 7436.
5 W. B. Hou and S. B. Cronin, *Adv. Funct. Mater.*, 2013, **23**, 1612.
6 W. X. Huang, Q. Hua and T. Cao, *Catal Lett*, 2014, **144**, 1355.
7 Q. F. Zhang, E. Uchaker, S. L. Candelaria and G. Z. Cao, *Chem. Soc. Rev.*, 2013, **42**, 3127.
8 M. Notarianni, K. Vernon, A. Chou, M. Aljada, J. Z. Liu and N. Motta, *Sol Energy*, 2014, **106**, 23.
9 J. N. Anker, W. P. Hall, O. Lyandres, N. C. Shah, J. Zhao and R. P. Van Duyne, *Nat. Mater.*, 2008, **7**, 442.
10 M. V. Kovalenko, L. Manna, A. Cabot, Z. Hens, D. V. Talapin, C. R. Kagan, V. I. Klimov, A. L. Rogach, P. Reiss, D. J. Milliron, P. Guyot-Sionnnest, G. Konstantatos, W. J. Parak, T. Hyeon, B. A. Korgel, C. B. Murray and W. Heiss, *ACS Nano*, 2015, **9**, 1012.
11 S. J. Tesh and T. B. Scott, *Adv. Mater.*, 2014, **26**, 6056.
12 G. Merle, M. Wessling and K. Nijmeijer, *J. Membrane Sci.*, 2011, **377**, 1.
13 A. Brouzgou, A. Podias and P. Tsiakaras, *J. Appl. Electrochem.*, 2013, **43**, 119.
14 A. V. Tripkovic, K. D. Popovic, B. N. Grgur, B. Blizanac, P. N. Ross and N. M. Markovic, *Electrochim. Acta*, 2002, **47**, 3707; C. W. Xu, H. Wang, P. K. Shen and S. P. Jiang, *Adv. Mater.*, 2007, **19**, 4256.
15 N. Ramaswamy and S. Mukerjee, *J. Phys. Chem. C*, 2011, **115**, 18015; I. Katsounaros, S. Cherevko, A. R. Zeradjanin and K. J. Mayrhofer, *Angew. Chem. Int. Ed.*, 2014, **53**, 102.
16 P. Rodriguez and M. T. M. Koper, *Phys. Chem. Chem. Phys.*, 2014, **16**, 13583; P. Rodriguez, Y. Kwon and M. T. M. Koper, *Nat. Chem.*, 2012, **4**, 177; Y. Kwon, S. C. S. Lai, P. Rodriguez and M. T. M. Koper, *J. Am. Chem. Soc.*, 2011, **133**, 6914.
17 S. M. Nie and S. R. Emery, *Science*, 1997, **275**, 1102; K. Kneipp, Y. Wang, H. Kneipp, L. T. Perelman, I. Itzkan, R. Dasari and M. S. Feld, *Phys. Rev. Lett.*, 1997, **78**, 1667.
18 C. Mohr and P. Claus, *Science progress*, 2001, **84**, 311.
19 H. Wei and H. X. Xu, *Nanoscale*, 2013, **5**, 10794.
20 Y. Wang, E. Laborda, K. Tschulik, C. Damm, A. Molina and R. G. Compton, *Nanoscale*, 2014, **6**, 11024.
21 M. Futamata, *Faraday Discuss.*, 2014, DOI: 10.1039/C4FD00188E.
22 T. A. El-Brolossy, T. Abdallah, M. B. Mohamed, S. Abdallah, K. Easawi, S. Negm and H. Talaat, *Eur Phys J-Spec Top*, 2008, **153**, 361.
23 P. D. Jadzinsky, G. Calero, C. J. Ackerson, D. A. Bushnell and R. D. Kornberg, *Science*, 2007, **318**, 430.
24 J. C. Gifford, J. Bresee, C. J. Carter, G. Wang, R. J. Melander, C. Melander and D. L. Feldheim, *Chem. Commun.*, 2014, **50**, 15860; J. Fontana, J. Naciri, R. Rendell and B. R. Ratna, *Adv. Opt. Mater.*, 2013, **1**, 100; M. Perfetti, F. Pineider, L. Poggini, E. Otero, M. Mannini, L. Sorace, C. Sangregorio, A. Cornia and R. Sessoli, *Small*, 2014, **10**, 323; U. Y. Lee, Y. S. Youn, J. Park and E. S. Lee, *ACS Nano*, 2014, **8**, 12858.
25 M. Kerker, O. Siiman, L. A. Bumm and D. S. Wang, *Appl. Optics*, 1980, **19**, 3253.
26 M. Schlesinger and M. Paunovic, *Modern electroplating*, Wiley, Hoboken, NJ, 5th edn., 2010.
27 D. Pletcher and F. Walsh, *Industrial electrochemistry*, Blackie Academic & Professional, London ; New York, 2nd edn., 1993.
28 C. Lee, J. Y. Kwak and F. C. Anson, *Anal. Chem.*, 1991, **63**, 1501.
29 E. M. El-Giar, R. A. Said, G. E. Bridges and D. J. Thomson, *J. Electrochem. Soc.*, 2000, **147**, 586; T. Danieli and D. Mandler, *J. Solid State Electrochem.*, 2013, **17**, 2989.
30 A. J. Bard and M. V. Mirkin, *Scanning electrochemical microscopy*, CRC Press, Boca Raton, Fla., 2nd edn., 2012.
31 S. Meltzer and D. Mandler, *J. Electrochem. Soc.*, 1995, **142**, L82; E. Ammann and D. Mandler, *J. Electrochem. Soc.*, 2001, **148**, C533; X. Xu, J. Jia, X. Yang and S. Dong, *Langmuir*, 2010, **26**, 7627; T. Danieli, J. Colleran and D. Mandler, *Phys. Chem. Chem. Phys.*, 2011, **13**, 20345; R. G. Fedorov and D. Mandler, *Phys. Chem. Chem. Phys.*, 2013, **15**, 2725.
32 T. Danieli, N. Gaponik, A. Eychmueller and D. Mandler, *J. Phys. Chem. C*, 2008, **112**, 8881; E. Malel and D. Mandler, *J. Electrochem. Soc.*, 2008, **155**, D459; M. Sheffer and D. Mandler, *Electrochim. Acta*, 2009, **54**, 2951; E. Malel, R. Ludwig, L. Gorton and D. Mandler, *Chem.-Eur. J.*, 2010, **16**, 11697; A. P. O'Mullane, S. J. Ippolito, A. M. Bond and S. K. Bhargava, *Electrochem. Commun.*, 2010, **12**, 611.
33 N. Urbanska, M. Pietraszkiewicz and J. Waluk, *J. Porphyr. Phthalocyanines*, 2007, **11**, 596.
34 J. Herrera Galeo, C. E. Castellano, A. J. Calandra and A. J. Ariva, *J. Electroanal. Chem.*, 1975, **66**, 207; R. P. Frankenthal and D. J. Siconolfi, *J. Electrochem. Soc.*, 1982, **129**, 1192; G.

Kelsall, N. J. Welham and M. A. Diaz, *J. Electroanal. Chem.*, 1993, **361**, 13; A. Kolics, A. E. Thomas and A. Wieckowski, *J. Chem. Soc., Faraday Trans.*, 1996, **92**, 3727.

35 J. Q. Liu and M. J. Nicol, *Can. Metall. Quart.*, 2002, **41**, 409.

36 C. H. Xiang, Q. J. Xie, J. M. Hu and S. Yao, *J. Electroanal. Chem.*, 2005, **584**, 201.

37 Z. L. Li, T. H. Wu, Z. J. Niu, W. Huang and H. D. Nie, *Electrochem. Commun.*, 2004, **6**, 44; K. Watling, G. A. Hope and R. Woods, *J. Electrochem. Soc.*, 2005, **152**, D103.

38 C. H. Gammons, Y. M. Yu and A. E. WiliamsJones, *Geochim. Cosmochim. Acta*, 1997, **61**, 1971.

39 J. Velmurugan, J.-M. Noel, W. Nogala and M. V. Mirkin, *Chem. Sci.*, 2012, **3**, 3307.

40 C. C. Pla Cid, E. R. Spada and M. L. Sartorelli, *Appl. Surf. Sci.*, 2013, **273**, 603.

41 B. Liu and A. J. Bard, *J. Phys. Chem. B*, 2002, **106**, 12801.

42 J. C. Stockert, M. Canete, A. Juarranz, A. Villanueva, R. W. Horobin, J. Borrell, J. Teixido and S. Nonell, *Curr Med Chem*, 2007, **14**, 997.

43 T. Kumagai, F. Hanke, S. Gawinkowski, J. Sharp, K. Kotsis, J. Waluk, M. Persson and L. Grill, *Phys. Rev. Lett.*, 2013, **111**; T. Kumagai, F. Hanke, S. Gawinkowski, J. Sharp, K. Kotsis, J. Waluk, M. Persson and L. Grill, *Nat. Chem.*, 2014, **6**, 41.

44 W. Nogala, K. Szot, M. Burchardt, F. Roelfs, J. Rogalski, M. Opallo and G. Wittstock, *Analyst*, 2010, **135**, 2051.

45 E. Blackie, E. C. Le Ru, M. Meyer, M. Timmer, B. Burkett, P. Northcote and P. G. Etchegoin, *Phys. Chem. Chem. Phys.*, 2008, **10**, 4147.

Nanoscale Accepted Manuscript